APPLICATION OF THE PARTIALLY-AVERAGED NAVIER-STOKES MODEL TO THE INVERSE CHEVRON SHOCK TUBE CONFIGURATION

Jérémie A. Janin
Los Alamos National Laboratory
Los Alamos, NM 87545, USA
jjanin@lanl.gov

Chad D. Meyer
Los Alamos National Laboratory
Los Alamos, NM 87545, USA
chadmeyer@lanl.gov

Juan A. Saenz
Los Alamos National Laboratory
Los Alamos, NM 87545, USA
juan.saenz@lanl.gov

Daniel M. Israel
Los Alamos National Laboratory
Los Alamos, NM 87545, USA
dmi1@lanl.gov

ABSTRACT

This work evaluates the PANS-BHR turbulence model for shock-driven mixing in the inverse chevron shock tube, focusing on the mixing parameter and turbulent kinetic energy. Several modeling strategies are assessed against a high-resolution implicit large-eddy simulation reference. The results show that the model can correctly predict the mixing parameter, even at low effective physical resolution. Among the strategies considered, applying the PANS methodology only to the turbulent kinetic energy and length-scale equations provides the most consistent agreement.

INTRODUCTION

The inverse chevron shock tube experiment has been studied for the past two decades (Hahn *et al.*, 2011; Haines *et al.*, 2013; West *et al.*, 2024). This configuration is a planar shock tube with three gas layers aligned horizontally (Fig. 1). As the shock wave passes through the membrane separating the two fluids, baroclinic vorticity is deposited at the interface, triggering Richtmyer–Meshkov instabilities and ultimately causing transition to turbulence. At later times, the inclined material interface gives rise to shear instabilities.

The resulting flow is unsteady and spans a broad range of evolving scales, so large-eddy simulation (LES) is the current state-of-the-art approach for resolving these phenomena. However, in practice, most LES are under-resolved, raising questions about the reliability of key quantities of interest. Alternatively, Reynolds-averaged Navier-Stokes (RANS) modeling, as in the BHR family of models (Besnard *et al.*, 1992), fully models turbulence effects. Using statistical homogeneity in the spanwise direction, the problem can be reduced to two spatial dimensions, reducing computational cost. Haines *et al.* (2013) showed that the BHR model predicts well the resolved integral mixing parameter. In this work, we employ a bridging model that resolves large energetic motions while modeling the sub-filter scales, thereby combining the strengths of LES and RANS. The results are compared with a high-resolution implicit LES (ILES) with a grid spacing of $1/64\,\mathrm{cm}$, the finest resolution reported to date for this configuration (~ 2.6 billion grid points).

GOVERNING EQUATIONS

This section presents the governing equations. Instantaneous quantities are denoted by a star, *e.g.* $\phi^\star$, while filtered quantities are denoted by a tilde $\tilde{\phi}$. To distinguish between standard filtered velocities, *i.e.* $\tilde{U}_i$, and Favre (density-weighted) filtered velocities, we use a separate notation for the latter. The Favre-filtered velocity is defined by $\tilde{\rho}\tilde{V}_i = \left\langle \rho^\star u_i^\star \right\rangle$, where $\langle . \rangle$ denotes a general filtering operator. The Favre-filtered mass fraction and total energy are denoted, respectively, as $\tilde{\rho}\tilde{Y}_i = \left\langle \rho^\star Y_i^\star \right\rangle$ and $\tilde{\rho}\tilde{E}_i = \langle \rho^\star E^\star \rangle$. Applying a linear, constant-preserving filter gives the following filtered Navier-Stokes equations (neglecting molecular viscosity and molecular diffusion):

Mass fraction

$$\frac{\partial \tilde{\rho}\tilde{Y}^n}{\partial t} + \frac{\partial \tilde{V}_j \tilde{\rho}\tilde{Y}^n}{\partial x_j} = -\frac{\partial \tilde{J}_j^n}{\partial x_j}, \quad \tilde{\rho} = \sum_n \tilde{\rho}\tilde{Y}^n \tag{1}$$

In the above equation $\tilde{\rho}$ and $\tilde{Y}^n$ are, respectively, the resolved mixture density and the Favre-filtered mass fraction of material n. The mass fraction turbulent diffusivity flux of material n, $\tilde{J}_j^n$, is modeled with a gradient diffusion hypothesis:

$$\tilde{J}_j^n = -\frac{\tilde{\rho}\nu_u}{\sigma_c}\frac{\partial \tilde{Y}^n}{\partial x_j}, \tag{2}$$

and σ_c is the turbulent diffusion coefficient.

Momentum

$$\frac{\partial \tilde{\rho}\tilde{V}_i}{\partial t} + \frac{\partial \tilde{\rho}\tilde{V}_i\tilde{V}_j}{\partial x_j} = -\frac{\partial \tilde{P}}{\partial x_i} - \frac{\partial \tilde{\rho}\tau_{ij}^1\left(u_i^\star, u_j^\star\right)}{\partial x_j} \tag{3}$$

In this equation, $\tilde{P}$ is the resolved pressure, and $\tau_{ij}^1\left(u_i^\star, u_j^\star\right)$ denotes the sub-filter stresses, expressed as generalized central second moments. The sub-filter stresses are modeled using the Boussinesq closure with a sub-filter eddy viscosity ν_u:

$$\tau_{ij}^1\left(u_i^\star, u_j^\star\right) = \left\langle \rho^\star u_i^\star u_j^\star \right\rangle / \tilde{\rho} - \tilde{V}_i\tilde{V}_j = -2\nu_u \tilde{S}_{ij} + \frac{2}{3}k_u\delta_{ij}, \tag{4}$$

where k_u is the sub-filter turbulent kinetic energy and $\tilde{S}_{ij}$ is the resolved strain-rate tensor,

$$\tilde{S}_{ij} = \frac{1}{2}\left(\frac{\partial \tilde{V}_i}{\partial x_j} + \frac{\partial \tilde{V}_j}{\partial x_i}\right). \tag{5}$$

The turbulent viscosity is evaluated using a RANS/LES bridging method, described in the next section.

Total energy: $\tilde{\rho}\tilde{E} = \tilde{\rho}\tilde{e} + 1/2\tilde{\rho}\tilde{V}_i\tilde{V}_i + k_u$

$$\begin{aligned}\frac{\partial \tilde{\rho}\tilde{E}}{\partial t} + \frac{\partial \tilde{V}_j\tilde{\rho}\tilde{E}}{\partial x_j} &= -\frac{\partial \tilde{P}\tilde{V}_j}{\partial x_j} - \frac{\partial \tilde{\rho}\tilde{V}_i\tau^1_{ij}(u^\star_i, u^\star_j)}{\partial x_j} \\ &+ \frac{\partial}{\partial x_j}\left[\frac{\mu_u}{\sigma_k}\frac{\partial k_u}{\partial x_j}\right] - \frac{\partial}{\partial x_j}\left[c_p \frac{\mu_u}{Pr_t}\frac{\partial \tilde{T}}{\partial x_j}\right] - \frac{\partial}{\partial x_j}\left[\sum_n h^n \tilde{J}^n_j\right]\end{aligned} \tag{6}$$

In the above equation, $\tilde{T}$, $\tilde{e}^n$, $\tilde{h}^n$ are respectively the filtered temperature, the internal energy and the enthalpy of material n. The turbulent Prandtl number is defined as $Pr_t = c_v\nu_u/\kappa$, κ is the effective thermal conductivity and c_v is the constant specific heat. Finally, an ideal-gas assumption is adopted, and pressure-temperature equilibrium is assumed at the cell level ($\tilde{P} = \tilde{P}^n = \tilde{P}^{n+1}$ and $\tilde{T}^n = \tilde{T}^{n+1}$), with:

$$\tilde{P} = (\gamma - 1)\tilde{\rho}\left(\tilde{E} - \frac{1}{2}\tilde{V}_i\tilde{V}_i - k_u\right), \tag{7}$$

where γ is the ratio of specific heats.

METHODOLOGY

Bridging models provide a seamless transition between Reynolds-averaged Navier–Stokes (RANS) and direct numerical simulation (DNS), thus covering the full spectrum from fully modeled to fully resolved turbulence. Within this framework, the Partially Averaged Navier–Stokes (PANS) methodology (Girimaji, 2005) provides a procedure in which the sub-filter transport equations are derived directly from the underlying RANS model, ensuring consistency while allowing variable resolution. The original PANS formulation introduces the turbulent kinetic energy ratio, defined as the ratio of unresolved to total turbulent kinetic energy. When this ratio equals unity, the model reduces to RANS, whereas as the ratio approaches zero, the method converges to DNS, realizing the concept of *accuracy on demand* (Germano (1992), Saenz *et al.* (2021), Grinstein *et al.* (2025)). The prescribed turbulent kinetic energy ratio f_k controls the effective physical resolution of the simulation.

The PANS methodology has been extended to variable-density flows by Pereira *et al.* (2021*b*). Specifically, the approach was applied to the one-point, linear eddy-viscosity model (LEVM) formulation of the Besnard-Harlow-Rauenzahn (BHR) model (Besnard *et al.*, 1992). In addition to the standard two-equation formulation for turbulent kinetic energy, k, and the dissipation rate, ε (with the length scale S serving as the second variable in the BHR model), Pereira *et al.* (2021*b*) generalized the PANS framework to include the transport equations for the density-velocity correlation, a_i, and the density-specific-volume covariance, b. Accordingly, the authors introduced two additional ratios of unresolved-to-total quantities, yielding the following set of control parameters:

$$f_k \equiv \frac{k_u}{k_t}, \quad f_\varepsilon \equiv \frac{\varepsilon_u}{\varepsilon_t}, \quad f_{a_i} \equiv \frac{a_{i_u}}{a_{i_t}}, \quad f_b \equiv \frac{b_u}{b_t}, \tag{8}$$

where the subscripts u and t denote unresolved and total components, respectively. The PANS BHR-LEVM closure thus provides transport equations for the following sub-filter quantities:

Turbulent kinetic energy

$$\begin{aligned}\frac{\partial \tilde{\rho}k_u}{\partial t} + \frac{\partial \tilde{V}_j\tilde{\rho}k_u}{\partial x_j} =& P_{b_u} + P_{s_u} + \frac{\partial}{\partial x_j}\left(\frac{\tilde{\rho}\nu_u}{\sigma_k}\frac{f_\varepsilon}{f_k^2}\frac{\partial k_u}{\partial x_j}\right) \\ & - \tilde{\rho}\frac{k_u^{3/2}}{S_u}\end{aligned} \tag{9}$$

Length-scale

$$\begin{aligned}\frac{\partial \tilde{\rho}S_u}{\partial t} + \frac{\partial \tilde{V}_j\tilde{\rho}S_u}{\partial x_j} =& \frac{S_u}{k_u}\left(c_4 P_{b_u} + c_1 P_{s_u}\right) \\ & + \frac{\partial}{\partial x_j}\left(\frac{\tilde{\rho}\nu_u}{\sigma_S}\frac{f_\varepsilon}{f_k^2}\frac{\partial S_u}{\partial x_j}\right) - c_2^\star\tilde{\rho}\sqrt{k_u}\end{aligned} \tag{10}$$

with

$$c_2^\star = c_2\frac{f_k}{f_\varepsilon} + (c_4 w_b + c_1 w_s)\left(1 - \frac{f_k}{f_\varepsilon}\right) \tag{11}$$

Density–velocity correlation

$$\begin{aligned}\frac{\partial \tilde{\rho}a_{i_u}}{\partial t} + \frac{\partial \tilde{V}_j\tilde{\rho}a_{i_u}}{\partial x_j} =& f_{a_i}\frac{b_u}{f_b}\frac{\partial \tilde{P}}{\partial x_i} + \frac{f_{a_i}}{f_k}\tau^1(u^\star_i, u^\star_j)\frac{\partial \tilde{\rho}}{\partial x_j} \\ & - \frac{f_{a_i}}{f_{a_j}}\tilde{\rho}a_{j_u}\frac{\partial \tilde{V}_i}{\partial x_j} + \frac{\tilde{\rho}}{f_{a_j}}\frac{\partial a_{i_u}a_{j_u}}{\partial x_j} \\ & - c_{a_1}\tilde{\rho}a_{i_u}\frac{\sqrt{k_u}}{S_u}\frac{f_k}{f_\varepsilon} + \frac{\partial}{\partial x_j}\left(\frac{\tilde{\rho}\nu_u}{\sigma_a}\frac{f_\varepsilon}{f_k^2}\frac{\partial a_{i_u}}{\partial x_j}\right)\end{aligned} \tag{12}$$

Density–specific-volume covariance

$$\begin{aligned}\frac{\partial \tilde{\rho}b_u}{\partial t} + \frac{\partial \tilde{V}_j\tilde{\rho}b_u}{\partial x_j} =& 2\tilde{\rho}\frac{a_{j_u}}{f_{a_j}}\frac{\partial b_u}{\partial x_j} - 2\frac{a_{j_u}}{f_{a_j}}(b_u + f_b)\frac{\partial \tilde{\rho}}{\partial x_j} \\ & - c_b\tilde{\rho}b_u\frac{f_k}{f_\varepsilon}\frac{\sqrt{k_u}}{S_u} + \tilde{\rho}^2\frac{\partial}{\partial x_j}\left(\frac{\nu_u}{\tilde{\rho}\sigma_b}\frac{f_\varepsilon}{f_k^2}\frac{\partial b_u}{\partial x_j}\right)\end{aligned} \tag{13}$$

In the above equations, the production of k_u by buoyancy and shear mechanisms are defined as:

$$P_{b_u} = a_{j_u}\frac{\partial \tilde{P}}{\partial x_j}, \quad P_{s_u} = -\tilde{\rho}\tau^1\left(u^\star_i, u^\star_j\right)\frac{\partial \tilde{V}_i}{\partial x_j}, \tag{14}$$

and the turbulent viscosity writes as:

$$\nu_u = c_\mu\sqrt{k_u}S_u. \tag{15}$$

As in the original PANS formulation, the ratios f_k and f_ε appear in the transport equations for sub-filter turbulent kinetic energy and dissipation. In contrast, the transport equations governing a_i and b involve all four ratios.

Pereira *et al.* (2021*a*) applied the PANS BHR-LEVM framework to the Rayleigh-Taylor configuration and investigated three strategies for prescribing the ratios. All strategies use constant ratios in time and space to avoid any commutation errors (Grinstein *et al.*, 2025). In this work, these strategies are assessed on the inverse chevron configuration, where the ratio f_k is always prescribed, while the other ratios are determined consistently as functions of f_k. The prescribed values for f_k are [0.25, 0.35, 0.50]. Following Pereira *et al.* (2021*a*), the strategies considered are:

S1: $f_\varepsilon = 1$; $f_b = 1$ and $f_{a_i} = 1$,
S2: $f_\varepsilon = 1$; $f_b = 1$ and $f_{a_i} = \sqrt{f_k}$,
S3: $f_\varepsilon = 1$; $f_b = f_k$ and $f_{a_i} = f_k/2$.

In addition, a strategy denoted $S4$ is introduced, in which the PANS methodology is applied only to the k and S equations, while no such modification is performed for a_i and b. The motivation for this strategy stems from the hypothesis that modifying only the turbulent kinetic energy and dissipation equations is sufficient, while a_i and b naturally adjust to the appropriate sub-filter quantities.

NUMERICAL SETUP

Three-dimensional simulations are carried out using the flow solver `xRAGE` (Gittings *et al.*, 2008). In addition to solving the six closure model equations (Eqs. (9)–(13)), this code employs a finite-volume formulation to solve the compressible, multi-material conservation equations for mass fraction (Eq. (1)), momentum (Eq. (3)) and energy (Eq. (6)). The governing equations are solved using the Harten–Lax–van Leer–Contact (HLLC) Riemann solver (Toro *et al.*, 1994) with a directionally unsplit strategy, direct remap, parabolic reconstruction (Colella & Woodward, 1984), and the low-Mach-number correction (LMC) proposed by Thornber *et al.* (2008). Spatial discretization is second-order accurate and based on a Godunov scheme, while the temporal discretization relies on an explicit Runge-Kutta scheme known as Heun's method. The time step, Δt, is set by prescribing a maximum instantaneous Courant–Friedrichs–Lewy (CFL) number of 0.8 according to

$$\Delta t = \frac{\Delta x \times CFL}{3\left(|V| + c\right)}, \tag{16}$$

where c denotes the local speed of sound and $|V|$ the velocity magnitude. The results are compared against simulations performed with `RIOT`, a multiphysics code built on top of `PARTHENON` (Grete *et al.*, 2022), which employs a similar unsplit-LMC strategy as in `xRAGE`. All simulations use uniform grids. PANS simulations are performed with $\Delta = 1/16\,\mathrm{cm}$ and are run to $4\,\mathrm{ms}$. Following Haines *et al.* (2013), we activate and initialize the turbulence model equations at $1.7\,\mathrm{ms}$, just after the first reshock ($k_0 = 10^5 f_k\,\mathrm{cm}^2/\mathrm{s}^2$, $S_0 = 0.25 f_k^{3/2}\,\mathrm{cm}$). The temporal evolution of the shock is shown in Fig. 2.

The inverse chevron configuration consists of a dense central layer of sulfur hexafluoride (SF_6), initially at rest, sandwiched between two quiescent air layers. This arrangement forms two material interfaces oriented normal to the direction of shock propagation. The computational domain is Cartesian with dimensions $L_x = 50\,\mathrm{cm}$, $L_y = 20\,\mathrm{cm}$, and $L_z = 10\,\mathrm{cm}$, where x, y, and z denote the streamwise, spanwise, and spannormal directions, respectively (cf. Fig. 1). The SF_6 layer

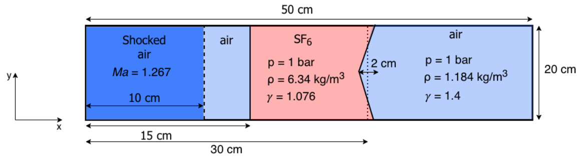

Figure 1: Illustration of the inverse chevron shock tube configuration used in the present work, with a spanwise extent of $L_z = 10\,\mathrm{cm}$.

extends from $x = 20\,\mathrm{cm}$ to $x = 35\,\mathrm{cm}$, forming interfaces at each boundary with the surrounding air. The downstream interface is modulated in the form of a chevron pattern with an amplitude of $2\,\mathrm{cm}$. The domain is periodic in the z-directions, while reflecting boundary conditions are imposed at the x and y-boundaries.

In this configuration, a shock wave with Mach number $M_s = 1.267$ is initialized in the leftmost air region and propagates rightward through the domain, sequentially crossing the two density interfaces. The shocked air region is defined using the Rankine–Hugoniot jump conditions, with the post-shock velocity computed based on upstream (unshocked) quantities. This results in a velocity of $u_1 = 136.9\,\mathrm{m/s}$, pressure $p_1 = 1.706\,\mathrm{bar}$, and density $\rho_1 = 1.726\,\mathrm{kg/m^3}$. Ahead of the shock, the unshocked air is at rest ($u_2 = 0\,\mathrm{m/s}$) and has pressure $p_2 = 1.0\,\mathrm{bar}$ and density $\rho_2 = 1.184\,\mathrm{kg/m^3}$. The interface separates the air from SF_6, which is assumed to be initially at a pressure of 1 bar, with density $\rho_{\mathrm{SF}_6} = 6.34\,\mathrm{kg/m^3}$, and a ratio of specific heats $\gamma = 1.076$.

Following Haines *et al.* (2013), the two air–SF_6 interfaces are initialized with perturbations that impose axial displacements about their nominal positions. The perturbation is constructed such that its derivative vanishes at the boundaries in the y-direction, while periodicity is enforced in the z-direction:

$$\eta(y,z) = \sum_{n=1}^{N}\sum_{m=0}^{M} S_n \left[a_{n,m}\cos(k_z^n z) + b_{n,m}\sin(k_z^n z) \right] \cos(k_y^m y) \tag{17}$$

in which $\kappa_y^m = \frac{\pi m}{L_y}$ and $\kappa_z^n = \frac{2\pi n}{L_z}$ are the components of the wave vector $\boldsymbol{\kappa}^{n,m}$, $a_{n,m}$ and $b_{n,m}$ are random coefficient following a normal distribution as $a_{n,m}, b_{n,m} \sim \mathcal{N}\left(0,1\right)$ to ensure a zero-mean perturbation, and finally S_n is the amplitude defined as $S_n = \sqrt{\alpha_n P(\kappa)\Delta\kappa_y\Delta\kappa_z}$, with α_n a coefficient to prescribe the desired standard deviation. In this study, $\sqrt{\langle \eta(y,z)^2 \rangle} = 0.01\,\mathrm{cm}$ as in Youngs (1991), Hahn *et al.* (2011), Haines *et al.* (2013) , West *et al.* (2024). The spectral slope can also be prescribed; here, a spectrum of the form $P(\kappa) = \kappa^{-2}$ has been adopted, consistent with observations from membrane-based interface characterization experiments (Barnes *et al.*, 2002).

QUANTITIES OF INTEREST

To compare the `xRAGE` PANS results with those obtained from ILES using `RIOT` on a fine grid ($\Delta x = 1/64\,\mathrm{cm}$), we first define the relevant quantities of interest (QOIs).

Mixing parameter

A key diagnostic is the mixing parameter, MIX, defined as

$$MIX = \rho^{\star 2} Y^\star_{SF_6} Y^\star_{air} \tag{18}$$

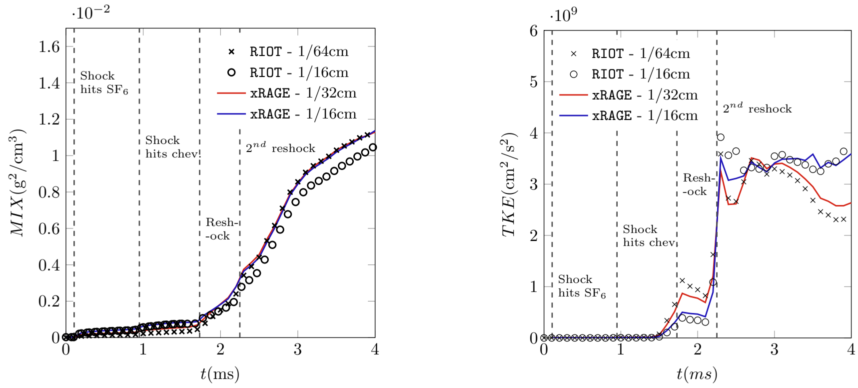

(a) (b)

Figure 2: Temporal evolution of the mixing parameter (left), computed with Eq. (18), and the TKE (right), computed with Eq. (25), both integrated over the entire domain. The shock position is also indicated. Symbols denote the `RIOT` ILES simulations, while solid lines correspond to the `xRAGE` ILES simulations.

where $\rho^\star$ denotes the instantaneous density, and $Y^\star_{SF_6}$ and $Y^\star_{air}$ denote the instantaneous mass fraction of SF_6 and air. This quantity is usually integrated over the entire volume and is of particular interest in inertial confinement fusion; further details can be found in Hahn *et al.* (2011) and Grinstein *et al.* (2026).

For the `RIOT` fine-grid simulations, *MIX* is evaluated directly from the instantaneous fields, under the assumption that the resolution is sufficient to fully resolve the relevant scales (Fig.2a). In contrast, for the `xRAGE` PANS simulations, subfilter contributions must be accounted for. To this end, subfilter fluctuations are denoted using double primes, defined as $\phi'' = \phi^\star - \widetilde{\phi}$.

To enable a consistent comparison between fine-grid ILES and PANS results, it is assumed that the filtering operation is idempotent and allows for an additive decomposition of the quantity into resolved and unresolved contributions, while preserving its total value. Accordingly,

$$MIX = \rho^{\star 2} Y^\star_{air} Y^\star_{SF_6} \approx \left\langle \rho^{\star 2} Y^\star_{air} Y^\star_{SF_6} \right\rangle \equiv MIX_{SRS}, \qquad (19)$$

where $\langle\cdot\rangle$ denotes the filtering operator associated with the scale-resolving formulation.

Ristorcelli (2017) derived an exact RANS formulation that incorporates unresolved effects through density variance and moments of density $\rho^\star$ and specific volume $v^\star = 1/\rho^\star$. In a SRS context, this derivation leads to the following exact expression:

$$MIX_{SRS} = \tilde{\rho}^2 \tilde{Y}_{SF_6}\left(1 - \tilde{Y}_{SF_6}\right) - \frac{(1+r)}{r^2}\tilde{\rho}^2 \left(\frac{b_u + 2b_u^2 - \overbrace{Sk_{SRS}\, b_u^{3/2}}^{I}}{(1+b_u)^2} + \frac{\overbrace{\left\langle \rho''^2 v''^2 \right\rangle}^{II}}{(1+b_u)^2} \right), \qquad (20)$$

where $r = \rho_{SF_6}/\rho_{air} - 1$ and ρ_{SF_6}, ρ_{air} are the material densities. The skewness term is expressed as:

$$Sk_{SRS} = \tilde{\rho}^{1/2} \frac{\left\langle \rho^\star Y''^{\,3}_{air} \right\rangle}{\left\langle \rho^\star Y''^{\,2}_{air} \right\rangle^{3/2}}. \qquad (21)$$

In Eq. (20), terms *I* and *II* require modeling. Following arguments similar to those presented in Ristorcelli (2017), the *MIX* parameter can be expressed only as a function of the concentration and the variable b obtained from the PANS-BHR model:

$$MIX_{SRS} = \tilde{\rho}^2 \tilde{Y}_{SF_6}\left(1 - \tilde{Y}_{SF_6}\right) - \tilde{\rho}^2 \frac{(1+r)}{r^2} \frac{b_u + (2+\chi) b_u^2 - Sk_{SRS} b_u^{3/2}}{(1+b_u)^2}. \qquad (22)$$

In the above equation, χ is a function of the filtered concentration $\langle Y^\star_{air} \rangle$ and is set to 1 here for practical reasons: this term diverges when the concentration tends to zero or one. It could also be approximated with its higher order terms, which leads to a small difference on the results. Finally, the skewness term reads as:

$$Sk_{SRS} b_u^{3/2} = 2\left(1 - 2\tilde{Y}_{air}\right) \frac{1-\theta}{2-\theta} \frac{r b_u}{1 + r\tilde{Y}_{air}}, \qquad (23)$$

and with

$$\theta = 1 - \frac{\frac{\left\langle \rho^\star Y''^{\,2}_{air} \right\rangle}{\tilde{\rho}}}{\tilde{Y}_{air}\left(1 - \tilde{Y}_{air}\right)}; \quad \frac{\left\langle \rho^\star Y''^{\,2}_{air} \right\rangle}{\tilde{\rho}} = \frac{b}{r^2}\left(1 + r\tilde{Y}_{air}\right)^2. \qquad (24)$$

The correction term, appearing on the right-hand side of Eq. (22), accounts for the contribution of unresolved scales.

Turbulent kinetic energy
The turbulent kinetic energy (TKE) is defined as

$$\bar{\rho} k = \frac{1}{2} \overline{\rho^\star u_i' u_i'}, \qquad (25)$$

where u_i' denotes the fluctuating velocity component, defined as $u_i' = u_i^\star - \overline{u_i^\star}$, and the overbar represents an averaging operation, taken here in the homogeneous z-direction (Fig.2b). The same hypothesis is made for the turbulent kinetic energy:

$$\bar{\rho} k \equiv \frac{1}{2} \overline{\rho^\star u_i' u_i'} \approx \frac{1}{2} \overline{\left\langle \rho^\star u_i' u_i' \right\rangle} \equiv \bar{\tilde{\rho}} k_{SRS}. \qquad (26)$$

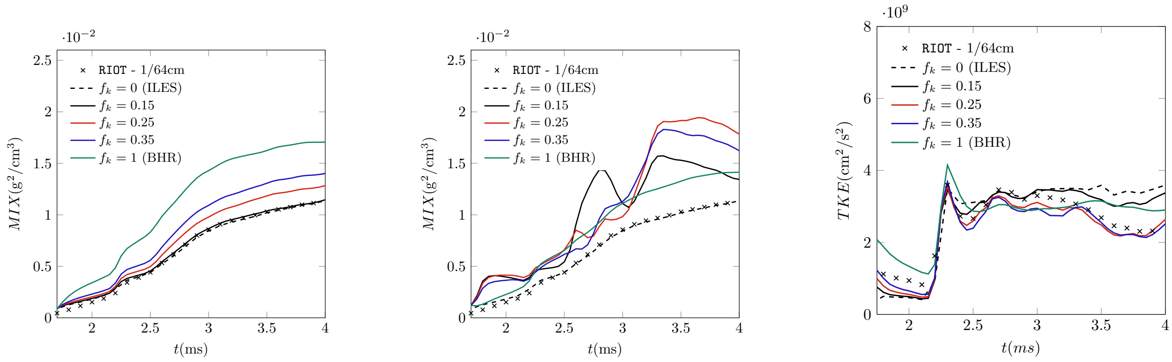

(a) (b) (c)

Figure 3: Temporal evolution of the integrated QOIs for S2 with $f_k = 0.25$ at grid resolution $\Delta = 1/16\,\mathrm{cm}$. MIX parameter (a) without the correction - Eq. (18), (b) with the correction term - Eq. (22) and (c) TKE.

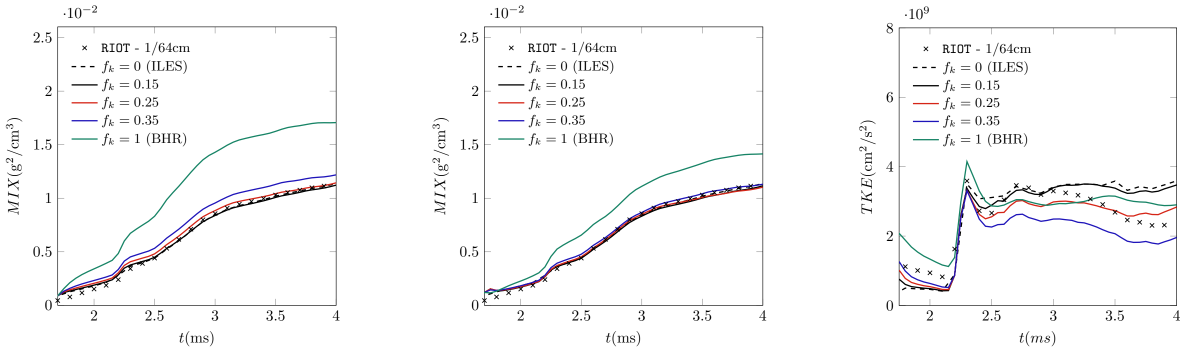

(a) (b) (c)

Figure 4: Temporal evolution of the integrated QOIs for S4 with $f_k = 0.25$ at grid resolution $\Delta = 1/16\,\mathrm{cm}$. MIX parameter (a) without the correction - Eq. (18), (b) with the correction term - Eq. (22) and (c) TKE.

In SRS, the total turbulent kinetic energy is a function of the fluctuating part, $\tilde{v}_i' = \tilde{V}_i - \overline{\tilde{V}}_i$,of the Favre filtered velocity, the density-velocity correlation a_i and the sub-filter turbulent kinetic energy k_u:

$$\overline{\rho} k_{SRS} = \frac{1}{2}\overline{\tilde{\rho}\,\tilde{v}_i'\tilde{v}_i'} + \overline{\tilde{\rho}\,\tilde{v}_i'\overline{a}_i} + \frac{1}{2}\overline{\tilde{\rho}\,\overline{a}_i\overline{a}_i} + \overline{\tilde{\rho} k_u}. \tag{27}$$

Overall, the *MIX* parameter introduces the density–specific-volume covariance b, while the TKE involves the density–velocity correlations a_i and the sub-filter turbulent kinetic energy k_u, thus ensuring a complete representation of the transported model quantities and allowing for a direct evaluation of how accurately these quantities are predicted.

RESULTS

In this section, the results for strategies 2 (Fig. 3) and 4 (Fig. 4) are presented for the MIX parameter and turbulent kinetic energy (TKE), both integrated over the entire domain. Strategies 1 and 3 are not shown, as they yield results similar to those of strategy 2. Fig. 3a and Fig. 3b show the MIX parameter without and with the correction term, respectively. In both cases, the model does not accurately predict the MIX parameter, and the correction term further degrades the results. This suggests that the quantity b is not accurately captured. Furthermore, decreasing the turbulent kinetic energy ratio does not lead to convergence toward the underlying ILES, contrary to what one would expect. The corresponding TKE for strategy 2 is shown in Fig. 3c.

The MIX parameter for strategy 4 is shown in Fig. 4a and Fig. 4b, without and with the correction term, respectively. As for S2, decreasing the turbulent kinetic energy ratio causes the MIX parameter to converge toward the ILES result ($f_k = 0$). In addition, the inclusion of the correction term significantly improves the prediction of the MIX parameter. The corresponding turbulent kinetic energy is shown in Fig. 4c, where it is correctly predicted for all values of the turbulent kinetic energy ratio, except in the BHR case ($f_k = 1$) and $f_k = 0.35$. Fig. 5 presents a two-dimensional slice of the MIX parameter integrated on z, included to show the effective resolution of the PANS-BHR simulations. It is evident that a substantial portion of the scales are unresolved for $f_k = 0.35$ compared to the $f_k = 0$ (ILES) case. Consistent with this observation, the energy spectrum (not shown) suggests that S4 with $f_k = 0.35$ has an effective resolution comparable to an ILES with $\Delta = 1/4\,\mathrm{cm}$.

CONCLUSION

The present results show that the PANS-BHR framework can predict shock-driven mixing in the inverse chevron configuration with encouraging accuracy, particularly for the MIX parameter. Among the strategies examined, the best performance is obtained when the PANS methodology is applied only to the turbulent kinetic energy and length-scale equations.

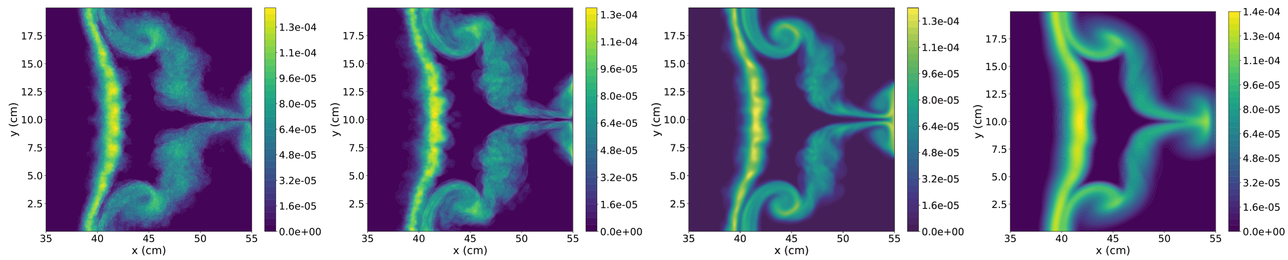

(a) (b) (c) (d)

Figure 5: MIX parameter integrated on z at $t = 3.4\,\mathrm{ms}$. a) ILES `RIOT` $\Delta x = 1/64\,\mathrm{cm}$, b) PANS $f_k = 0$ `xRAGE` $\Delta x = 1/16\,\mathrm{cm}$, c) PANS S4-$f_k = 0.35$ `xRAGE` $\Delta x = 1/16\,\mathrm{cm}$, d) PANS $f_k = 1$ `xRAGE` $\Delta x = 1/16\,\mathrm{cm}$.

In this case, the correction term improves the MIX prediction, although the turbulent kinetic energy remains underpredicted. Overall, the model remains effective at low physical resolution. Future work will examine the effects of grid and physical resolution using strategy 4.

ACKNOWLEDGMENTS

The authors gratefully acknowledge the Eulerian Codes Team at Los Alamos National Laboratory for their continuous support. This work was supported by the U.S. Department of Energy through the Los Alamos National Laboratory. Los Alamos National Laboratory is operated by Triad National Security, LLC, for the National Nuclear Security Administration of U.S. Department of Energy (Contract No. 89233218CNA000001).

REFERENCES

Barnes, C. W., Batha, S. H., Dunne, A. M., Magelssen, G. R., Rothman, S., Day, R. D., Elliott, N. E., Haynes, D. A., Holmes, R. L., Scott, J. M., Tubbs, D. L., Youngs, D. L., Boehly, T. R. & Jaanimagi, P. 2002 Observation of mix in a compressible plasma in a convergent cylindrical geometry. *Proceedings of the Ninth International Workshop on the Physics of Compressible Turbulent Mixing* **9**, 4431.

Besnard, D., Harlow, F. H. & Zemach, R. M. Rauenzahn C. 1992 Turbulence transport equations for variable-density turbulence and their relationship to two-field models. *Tech. Rep. LA-12303-MS* **DE92**, 017292.

Colella, P. & Woodward, P. R. 1984 The piecewise parabolic method (ppm) for gas-dynamical simulations. *Journal of Computational Physics* **54**, 174.

Germano, M. 1992 Turbulence: the filtering approach. *Journal of Fluid Mechanics* **238**, 325–336.

Girimaji, S. S. 2005 Partially-averaged navier-stokes model for turbulence: A reynolds-averaged navier-stokes to direct numerical simulation bridging method. *Journal of Applied Mechanics* **73**, 413421.

Gittings, M., Weaver, R., Clover, M., Betlach, T., Byrne, N., Coker, R., Dendy, E., Hueckstaedt, R., New, K., Oakes, W. R., Ranta, D. & Stefan, R. 2008 The rage radiation-hydrodynamic code. *Computational Science Discovery* **1**, 015005.

Grete, P., Dolence, J. C., Miller, J. M., Brown, J., Ryan, B., Gaspar, A., Swaminarayan, S., Lippuner, J., Solomon, C. J., Shipman, G., Junghans, C., Holladay, D., Stone, J. M. & Roberts, L. F. 2022 Parthenon—a performance portable block-structured adaptive mesh refinement framework. *The International Journal of High Performance Computing Applications* **37**, 465–486.

Grinstein, F, Chiravalle, P & Greene, R. K. 2026 Recent progress on coarse graining simulations. *Physica D: Nonlinear Phenomena* **489**, 135116.

Grinstein, F. F., Pereira, F. S. & Germano, M., ed. 2025 *Coarse Graining Turbulence: Modeling and Data-Driven Approaches and their Applications*. Cambridge: Cambridge University Press.

Hahn, M., Drikakis, D., Youngs, D.L. & Williams, R.J.R 2011 Richtmyer–meshkov turbulent mixing arising from an inclined material interface with realistic surface perturbations and reshocked flow. *Phys. Fluids* **23**, 046101.

Haines, B.M., Grinstein, F.F. & Schwarzkopf, J.D. 2013 Reynolds-averaged navier–stokes initialization and benchmarking in shock-driven turbulent mixing. *J. Turbul.* **14**, 46–70.

Pereira, F. S., Grinstein, F. F., Israel, D. M., Rauenzahn, R. & Girimaji, S. S. 2021*a* Modeling and simulation of transitional rayleigh–taylor flow with partially averaged navier–stokes equations. *Phys. Fluids* **33**, 115118.

Pereira, F. S., Grinstein, F. F., Israel, D. M., Rauenzahn, R. & Girimaji, S. S. 2021*b* Partially averaged navier-stokes closure modeling for variable density turbulent flow. *Phys. Rev. Fluids* **6**, 084602.

Ristorcelli, J. R. 2017 Exact statistical results for binary mixing and reaction in variable density turbulence. *Phys. Fluids* **29**, 020705.

Saenz, J. A., Aslangil, D. & Livescu, D. 2021 Filtering, averaging, and scale dependency in homogeneous variable density turbulence. *Phys. Fluids* **33**, 025115.

Thornber, B., Mosedale, A., Drikakis, D., Youngs, D. & Williams, R. J. R. 2008 An improved reconstruction method for compressible flows with low mach number features. *Journal of Computational Physics* **227**, 4873.

Toro, E. F., Spruce, M. & Speares, W. 1994 Restoration of the contact surface in the hll-riemann solver. *Shock Waves* **4**, 25.

West, S. R., Sadler, J. D., Powell, P. D. & Zhou, Y. 2024 Shock-driven three-fluid mixing with various chevron interface configurations. *Phys. Fluids* **36**, 104132.

Youngs, D.L. 1991 Three-dimensional numerical simulation of turbulent mixing by rayleigh-taylor instability. *Phys. Fluids A* **3**, 1312.